Controllability Study of Two-Wheel Robot for Nonlinear Optimal Control and Implementation

KOKKRATHOKE, S and XU, Xu <http://orcid.org/0000-0002-9721-9054>

Controllability Study of Two-Wheel Robot for Nonlinear Optimal Control and Implementation

Surapong Kokkrathoke
Department of Engineering and Mathematics
Sheffield Hallam University
Sheffield, UK
surapong.kokkrathoke@student.shu.ac.uk

Xu Xu
Department of Engineering and Mathematics
Sheffield Hallam University
Sheffield, UK
xu.xu@shu.ac.uk

***Abstract*—This paper presents the benefits of controllability study, used to facilitate the implementation of a nonlinear optimal controller. The controllability technique can be applied to investigate the controllable ranges of different state-space models from the same physical system. Once the controllability of each mathematical model is established, controllable parts from different models are selected to build a new joint model before implementing the nonlinear freezing optimal control and extended Kalman filter. When applied to a two-wheel LEGO EV3 robot, the novel mixing model demonstrates excellent stabilising control results compared against both previous models by: 1) producing smoother transient behaviour with less oscillations and 2) demonstrating a broader initial pitch angle range for stabilisation using a nonlinear optimal controller.**

Keywords—Two-wheel balancing robot, optimal control, nonlinear control, extended Kalman filter, controllability

I. INTRODUCTION

All physical systems are nonlinear systems and the main benefit of adopting any nonlinear control method is that nonlinear systems can be controlled globally (i.e., linearisation around the operating point is no longer necessary). The nonlinear freezing optimal control (NFOC), introduced by Banks and Mhana in [1], is an advanced nonlinear controller that extends the linear quadratic regulator by 'freezing' the system's state space matrix at every time step for the calculation of control gains. A number of studies and applications of the NFOC have been presented in recent years, for example, the single inverted pendulum on a cart [2], the multilink inverted pendulum on a cart [3], the simulation [4] and implementation [5] of a self-balancing two-wheel robot. Moreover, the NFOC is also known as state-dependent Riccati equation (SDRE) control. For instance, the implementation of the F-8 aircraft flight controller used an SDRE technique presented in [6].

Furthermore, the NFOC controller has been combined with a signal filtering and state estimation technique, named extended Kalman filter (EKF). It has been applied to improve the accuracy of feedback control. The combination of the NFOC with EKF has been utilised in many applications, for example, the estimation of missile trajectory guidance [7], drug delivery in cancer treatment by estimating the number of normal cells [8], and additionally, the reduction of external disturbance noise in flexible-joint of the robotic arm [9].

In this research, a two-wheel robot (TWR), namely, LEGO EV3, is stabilised by the application of the nonlinear freezing optimal control with an extended Kalman filter. As presented in the previous work [5], the NFOC with EKF demonstrated superior results compared with the linear optimal control (LOC) and the NFOC without Kalman filter, i.e., the operating range of NFOC controlled TWR with EKF was most comprehensive and the EKF resolved the gyro sensor drift issue. Noticeably, the large operational range of TWR was demonstrated, because the linearisation is not a requirement, leading the system to be controlled globally.

Another advantage of adopting a nonlinear controller is that controllability study of system models can be performed and plotted as 3D or 2D cross-section graphs based on the evolution of the state vector to guide controller design. This technique can be applied to investigate the controllability range of different state-space models obtained from the same TWR prototype before implementation. For example, the benefits of the controllability test in 2D plots were analysed for the TWR model in [4]. In particular, in this study, the state variable of constraint voltage input introduced in [2] is included to reflect the restriction of the LEGO robot's motor voltage; hence, the controllability test matrix will present 3D plots as it has more state variables than the unconstrained voltage input model.

The rest of this paper is outlined as follows: in Section II, the dynamical system of TWR will be analysed, followed by different mathematical models of the same TWR set-up. Next, Section III will demonstrate the application of NFOC with EKF to the TWR. Then, in Section IV, the controllability test and simulation of the TWR model will be investigated. In Section V, the implementation results using a LEGO EV3 Robot will be presented and discussed. Finally, the conclusion will be given in Section VI.

II. MATHEMATICAL MODELS

The mathematical model is obtained from the TWR as shown in Fig. 1. This Lagrangian technique is used to create the state-space models as follows [4]:

$$\boldsymbol{L = T - V}, \tag{1}$$

$$\frac{\boldsymbol{d}}{\boldsymbol{dt}}\frac{\boldsymbol{\partial L}}{\boldsymbol{\partial \dot{x}_j}} - \frac{\boldsymbol{\partial L}}{\boldsymbol{\partial x_j}} = \boldsymbol{F_j},\ \boldsymbol{1 \le j \le n}, \tag{2}$$

where L, T and V are the Lagrangian expression, kinetic and potential energy, respectively ; the $\boldsymbol{x_j}$ is the generalised coordinate and $\boldsymbol{F_j}$ is the generalised force.

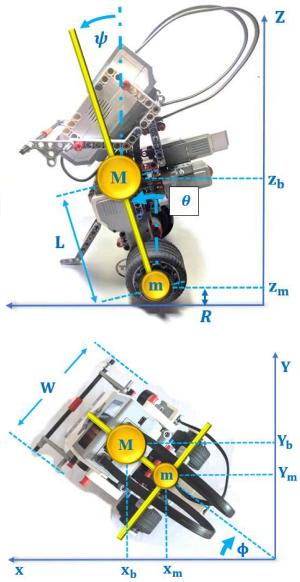

Fig. 1. A two-wheel robot with physical parameters

Therefore, the mathematical model of the LEGO EV3 robot can be represented as [10]:

$$[(2m+M)R^2+2J_w+2n^2J_m]\ddot{\theta}-MLR\dot{\psi}^2\sin\psi +(MLR\cos\psi-2n^2J_m)\ddot{\psi}=F_\theta, \quad (3)$$

$$(MLR\cos\psi-2n^2J_m)\ddot{\theta}+(ML^2+J_\psi+2n^2J_m)\ddot{\psi} -MgL\sin\psi-ML^2\dot{\phi}^2\sin\psi\cos\psi=F_\psi, \quad (4)$$

$$\left[\frac{1}{2}mW^2+J_\phi+\frac{W^2}{2R^2}(J_w+n^2J_m)+ML^2\sin^2\psi\right]\ddot{\phi} +2ML^2\dot{\psi}\,\dot{\phi}\sin\psi\cos\psi=F_\phi. \quad (5)$$

where $\boldsymbol{\theta}$, $\boldsymbol{\psi}$ and $\boldsymbol{\phi}$ are wheel angle, robot pitch angle, and robot yaw angle, respectively. Note, the coordinate $\boldsymbol{\phi}$ is neglected in this study and details of other parameters are presented in [5]. Moreover, the left ($v1$) and right ($v2$) motor voltages are added into Eqs. (3)-(5) and a tracking system design is utilised to decrease steady-state errors in the displacement of the LEGO EV3 robot. Then, the Eqs. (3)-(5) can be rewritten as the state-space representation of the system, as follows:

$$\dot{\boldsymbol{x}}_1=\boldsymbol{x}_2, \quad (6)$$

$$\dot{\boldsymbol{x}}_2=\frac{e_{m22}(x_3)}{(a+b(x_3))}\times\boldsymbol{x}_2+\frac{e_{23}(x_3)}{(a+b(x_3))x_3}\times\boldsymbol{x}_3+\frac{e_{m24}(x_3,x_4)}{(a+b(x_3))}\times\boldsymbol{x}_4 +\frac{f_{m21}}{(a+b(x_3))}\times v_1+\frac{f_{m22}(x_3)}{(a+b(x_3))}\times v_2, \quad (7)$$

$$\dot{\boldsymbol{x}}_3=\boldsymbol{x}_4, \quad (8)$$

$$\dot{\boldsymbol{x}}_4=\frac{e_{m42}(x_3)}{(a+b(x_3))}\times\boldsymbol{x}_2+\frac{e_{43}(x_3)}{(a+b(x_3))x_3}\times\boldsymbol{x}_3+\frac{e_{m44}(x_3,x_4)}{(a+b(x_3))}\times\boldsymbol{x}_4 +\frac{f_{m41}(x_3)}{(a+b(x_3))}\times\boldsymbol{v}_1+\frac{f_{m42}(x_3)}{(a+b(x_3))}\times\boldsymbol{v}_2, \quad (9)$$

$$\dot{x}_5=x_1, \quad (10)$$

where the generalised coordinates are given by:

$$x_1=\theta,\ x_2=\dot{\theta}\ \Rightarrow\ \dot{x}_2=\ddot{\theta},\ x_3=\psi,\ x_4=\dot{\psi}\ \Rightarrow\ \dot{x}_4=\ddot{\psi},$$

and x_5 is an integrator of x_1 applied to the tracking system.

Consequently, the nonlinear state-space matrix form of TWR, with a tracking design included, can be written as [4]:

Model A:

$$\begin{pmatrix}\dot{x}_1\\ \dot{x}_2\\ \dot{x}_3\\ \dot{x}_4\\ \dot{x}_5\end{pmatrix}=\begin{pmatrix}0 & 1 & 0 & 0 & 0\\ 0 & \frac{e_{m22}(x_3)}{a+b(x_3)} & \frac{e_{23}(x_3)}{[a+b(x_3)]x_3} & \frac{e_{m24}(x_3,x_4)}{a+b(x_3)} & 0\\ 0 & 0 & 0 & 1 & 0\\ 0 & \frac{e_{m42}(x_3)}{a+b(x_3)} & \frac{e_{43}(x_3)}{[a+b(x_3)]x_3} & \frac{e_{m44}(x_3,x_4)}{a+b(x_3)} & 0\\ 1 & 0 & 0 & 0 & 0\end{pmatrix}\times\begin{pmatrix}x_1\\ x_2\\ x_3\\ x_4\\ x_5\end{pmatrix} +\begin{pmatrix}0 & 0\\ \frac{f_{m21}(x_3)}{a+b(x_3)} & \frac{f_{m22}(x_3)}{a+b(x_3)}\\ 0 & 0\\ \frac{f_{m41}(x_3)}{a+b(x_3)} & \frac{f_{m42}(x_3)}{a+b(x_3)}\\ 0 & 0\end{pmatrix}\begin{pmatrix}v_1\\ v_2\end{pmatrix}. \quad (11)$$

The model given in Eq. (11) is named as Model A. Because state-space models are non-unique representations, other variations of nonlinear state-space models of the same TWR system exist. For example, different state-space representations (named Model B and Model C) can be created as below:

Model B:

$$\begin{pmatrix}\dot{x}_1\\ \dot{x}_2\\ \dot{x}_3\\ \dot{x}_4\\ \dot{x}_5\end{pmatrix}=\begin{pmatrix}0 & 1 & 0 & 0 & 0\\ 0 & \frac{e_{m22}(x_3)}{a+b(x_3)} & \frac{e_{23}(x_3)+e_{m24}(x_3,x_4)x_4}{[a+b(x_3)]x_3} & 0 & 0\\ 0 & 0 & 0 & 1 & 0\\ 0 & \frac{e_{m42}(x_3)}{a+b(x_3)} & \frac{e_{43}(x_3)+e_{m44}(x_3,x_4)x_4}{[a+b(x_3)]x_3} & 0 & 0\\ 1 & 0 & 0 & 0 & 0\end{pmatrix}\times\begin{pmatrix}x_1\\ x_2\\ x_3\\ x_4\\ x_5\end{pmatrix} +\begin{pmatrix}0 & 0\\ \frac{f_{m21}(x_3)}{a+b(x_3)} & \frac{f_{m22}(x_3)}{a+b(x_3)}\\ 0 & 0\\ \frac{f_{m41}(x_3)}{a+b(x_3)} & \frac{f_{m42}(x_3)}{a+b(x_3)}\\ 0 & 0\end{pmatrix}\begin{pmatrix}v_1\\ v_2\end{pmatrix}. \quad (12)$$

Model C:

$$\begin{pmatrix}\dot{x}_1\\ \dot{x}_2\\ \dot{x}_3\\ \dot{x}_4\\ \dot{x}_5\end{pmatrix}=\begin{pmatrix}0 & 1 & 0 & 0 & 0\\ 0 & \frac{e_{m22}(x_3)}{a+b(x_3)} & 0 & \frac{e_{23}(x_3)+e_{m24}(x_3,x_4)x_4}{a+b(x_3)x_4} & 0\\ 0 & 0 & 0 & 1 & 0\\ 0 & \frac{e_{m4}(x_3)}{a+b(x_3)} & 0 & \frac{e_{43}(x_3)+e_{m44}(x_3,x_4)x_4}{a+b(x_3)x_4} & 0\\ 1 & 0 & 0 & 0 & 0\end{pmatrix}\times\begin{pmatrix}x_1\\ x_2\\ x_3\\ x_4\\ x_5\end{pmatrix} +\begin{pmatrix}0 & 0\\ \frac{f_{m21}(x_3)}{a+b(x_3)} & \frac{f_{m22}(x_3)}{a+b(x_3)}\\ 0 & 0\\ \frac{f_{m41}(x_3)}{a+b(x_3)} & \frac{f_{m42}(x_3)}{a+b(x_3)}\\ 0 & 0\end{pmatrix}\begin{pmatrix}v_1\\ v_2\end{pmatrix}. \quad (13)$$

Although there are an infinite number of different but valid state-space models of the same TWR system, three example models are shown in this Section. Subsequently, these three models will be investigated using the controllability test in Section IV and then implemented in Section V.

III. CONTROLLER DESIGN

A. Nonlinear Freezing Optimal Control (NFOC)

In this research, the NFOC is applied to the TWR similar to the previous work [4], where the system can be written in the form of [1]:

$$\dot{\boldsymbol{x}} = \boldsymbol{A}(\boldsymbol{x})\boldsymbol{x} + \boldsymbol{B}(\boldsymbol{x})\boldsymbol{u}. \tag{14}$$

At every time step, the Linear Quadratic Regulator (LQR) is applied to optimise the TWR system, given by the nonlinear feedback control as follows [11]:

$$\boldsymbol{u} = -\boldsymbol{K}(\boldsymbol{x})\boldsymbol{x} = -\boldsymbol{R}^{-1}(\boldsymbol{x})\boldsymbol{B}^{\boldsymbol{T}}(\boldsymbol{x})\boldsymbol{P}(\boldsymbol{x})\boldsymbol{x}, \tag{15}$$

where $\boldsymbol{K}$ and $\boldsymbol{P}(\boldsymbol{x})$ are nonlinear feedback gain and algebraic matrix Riccati equation solution (see below), respectively.

$$\boldsymbol{A}^{\boldsymbol{T}}(\boldsymbol{x})\boldsymbol{P}(\boldsymbol{x}) + \boldsymbol{P}(\boldsymbol{x})\boldsymbol{A}(\boldsymbol{x}) + \boldsymbol{Q}(\boldsymbol{x}) - \boldsymbol{P}(\boldsymbol{x})\boldsymbol{B}(\boldsymbol{x})\boldsymbol{R}^{-1}(\boldsymbol{x})\boldsymbol{B}^{\boldsymbol{T}}(\boldsymbol{x})\boldsymbol{P}(\boldsymbol{x}) = \boldsymbol{0}\,. \tag{16}$$

B. Nonlinear Freezing Optimal Control with Extended Kalman Filter (NFOC with EKF)

In previous research [5], it was presented that the gyro sensor drift problem could be reduced with satisfactorily using an EKF; therefore, the NFOC with EKF has been selected to be applied to the LEGO EV3 robot in this study. Thus, the nonlinear system with an extended Kalman filler is given as [12]:

$$\dot{\boldsymbol{x}} = \boldsymbol{a}(\boldsymbol{x}, \boldsymbol{u}, \boldsymbol{t}) + \boldsymbol{G}(\boldsymbol{t})\boldsymbol{w}, \tag{17}$$

$$\boldsymbol{y} = \boldsymbol{c}(\boldsymbol{x}, \boldsymbol{t}) + \boldsymbol{v}, \tag{18}$$

where $\boldsymbol{w}$ and $\boldsymbol{v}$ are the process noise and measurement noise, respectively with $\boldsymbol{w} \sim (\boldsymbol{0},\ \boldsymbol{Q_k})$, $\boldsymbol{v} \sim (\boldsymbol{0},\ \boldsymbol{R_K})$, which $\boldsymbol{R_k}$ and $\boldsymbol{Q_k}$ are weighting matrices, and $\boldsymbol{G}$ is the process noise, which is used as $\boldsymbol{G} = \boldsymbol{I_{5\times5}}$.

Furthermore, the nonlinear system estimation can be written as:

$$\dot{\hat{\boldsymbol{x}}} = \boldsymbol{a}(\hat{\boldsymbol{x}}, \boldsymbol{u}, \boldsymbol{t}) + \boldsymbol{K_k}(\hat{\boldsymbol{x}}, \boldsymbol{t})(\boldsymbol{y} - \boldsymbol{c}(\hat{\boldsymbol{x}}, \boldsymbol{t}), \tag{19}$$

where $\boldsymbol{K_k}$ is the gain of Kalman filter and the Jacobian matrices are given by:

$$\boldsymbol{A}(\boldsymbol{x}, t) = \frac{\partial \boldsymbol{a}(\boldsymbol{x},\boldsymbol{u},t)}{\partial \boldsymbol{x}}, \boldsymbol{A}(\hat{\boldsymbol{x}}, t) = \frac{\partial \boldsymbol{a}(\hat{\boldsymbol{x}},\boldsymbol{u},t)}{\partial \hat{\boldsymbol{x}}}, \tag{20}$$

$$\boldsymbol{C}(\boldsymbol{x}, t) = \frac{\partial \boldsymbol{c}(\boldsymbol{x},t)}{\partial \boldsymbol{x}}, \boldsymbol{C}(\hat{\boldsymbol{x}}, t) = \frac{\partial \boldsymbol{c}(\hat{\boldsymbol{x}},t)}{\partial \hat{\boldsymbol{x}}}. \tag{21}$$

Thus, $\boldsymbol{K_k}$ is demonstrated as:

$$\boldsymbol{K_k}(\hat{\boldsymbol{x}}, t) = \boldsymbol{P_k}(\hat{\boldsymbol{x}}, t)\boldsymbol{C}^{\boldsymbol{T}}(\hat{\boldsymbol{x}}, t)\boldsymbol{R_k^{-1}}(\hat{\boldsymbol{x}}, t), \tag{22}$$

where equation $\boldsymbol{P_k}$ is the solution of algebraic Riccati, given by:

$$\boldsymbol{A}(\hat{\boldsymbol{x}}, \boldsymbol{t})\boldsymbol{P_k}(\hat{\boldsymbol{x}}, t) + \boldsymbol{P_k}(\hat{\boldsymbol{x}}, t)\boldsymbol{A}^{\boldsymbol{T}}(\hat{\boldsymbol{x}}, t) - \boldsymbol{P_k}(\hat{\boldsymbol{x}}, t)\boldsymbol{C}^{\boldsymbol{T}}(\hat{\boldsymbol{x}}, t)\boldsymbol{R_k^{-1}}(\hat{\boldsymbol{x}}, t)\boldsymbol{C}(\hat{\boldsymbol{x}}, t)\boldsymbol{P_k}(\hat{\boldsymbol{x}}, t) + \boldsymbol{Q_k}(\hat{\boldsymbol{x}}, t) = 0. \tag{23}$$

IV. SIMULATION RESULTS

In this subsection, mathematical models of the TWR obtained in Section II, the corresponding controllability tests and NFOC controller designs with EKF are simulated in MATLAB. Note, in this research, the weight matrices $\boldsymbol{Q}$, $\boldsymbol{R}$, $\boldsymbol{Q_k}$ and $\boldsymbol{R_k}$ are the same value as in [5]. Furthermore, the feedback control system ($\boldsymbol{u}$) in simulation should be considered by restricting at the maximum 8.3V similar to the power supply of LEGO EV3 (Further parameters of LEGO EV3 described in [5]). Additionally, the equation of nonlinear model needs to be modified to combine with constraint parameters, which the control input is given in [4],

$$\boldsymbol{u} = \begin{bmatrix} v_1 \\ v_2 \end{bmatrix} = \boldsymbol{\phi}(x_6) = \begin{bmatrix} \phi_L(x_6) \\ \phi_R(x_6) \end{bmatrix}. \tag{24}$$

Then, the new state variable x_6 is define as:

$$\dot{x}_6 = w_c.$$

Therefore, the TWR model with input constraint can be written as [2]:

$$\dot{\boldsymbol{x}}_{\boldsymbol{c}} = \begin{bmatrix} \dot{\boldsymbol{x}} \\ \dot{\boldsymbol{x}}_6 \end{bmatrix} = \begin{bmatrix} \boldsymbol{A}(\boldsymbol{x}) & \frac{\boldsymbol{B}(\boldsymbol{x})\boldsymbol{\phi}(\boldsymbol{x}_6)}{\boldsymbol{x}_6} \\ \boldsymbol{0}_{\boldsymbol{1}\times\boldsymbol{n}} & \boldsymbol{0} \end{bmatrix} \begin{bmatrix} \boldsymbol{x} \\ \boldsymbol{x}_6 \end{bmatrix} + \begin{bmatrix} \boldsymbol{0}_{\boldsymbol{n}\times\boldsymbol{1}} \\ \boldsymbol{1} \end{bmatrix} \boldsymbol{w}_{\boldsymbol{c}}, \tag{25}$$

where $\boldsymbol{w_c}$ is the scalar control input, and $\dot{\boldsymbol{x}}_{\boldsymbol{c}} = [\dot{\boldsymbol{x}}_{\boldsymbol{1}}, \dot{\boldsymbol{x}}_{\boldsymbol{2}}, \dot{\boldsymbol{x}}_{\boldsymbol{3}}, \dot{\boldsymbol{x}}_{\boldsymbol{4}}, \dot{\boldsymbol{x}}_{\boldsymbol{5}}, \dot{\boldsymbol{x}}_{\boldsymbol{6}}]^{\boldsymbol{T}}$. To make the control saturation $\boldsymbol{\phi}(\boldsymbol{x_6})$ smooth, these conditions are given as [2]:

$$\phi_L(x_6) = \phi_R(x_6) = \begin{cases} \lambda\ , & x_6 > \lambda \\ \lambda sin\,(\frac{\pi x_6}{2\lambda}), & |x_6| \geq \lambda, \\ -\lambda\ , & x_6 < -\lambda \end{cases} \tag{26}$$

where $\boldsymbol{\lambda}$ is the maximum of Lego EV3 motor at 8.3V and the cost function is represented as:

$$J = \frac{1}{2}\int_0^\infty [\boldsymbol{x_c}^{\boldsymbol{T}}\boldsymbol{Q_c}(\boldsymbol{x_c})\boldsymbol{x_c} + w_c^T\boldsymbol{R_a}(\boldsymbol{x_c})w_c]dt. \tag{27}$$

Moreover, the new weighting matrix $\boldsymbol{Q_c}$ can be written as:

$$\boldsymbol{Q_c} = \begin{bmatrix} \boldsymbol{Q} & 0 \\ 0 & \phi_L^2(x_6)2R_{11} \end{bmatrix}, \tag{28}$$

where $\boldsymbol{R_{11}}$ is 10. Additionally, the new weighting matrix $\boldsymbol{R_a}$ is selected as $\boldsymbol{R_a} = \boldsymbol{0.001}$, but this parameter is now a scalar similar to the new control input $\boldsymbol{w_c}$.

A: Controllability Test

As mentioned in Section II, the nonlinear system representations are non-unique. The rank of controllability matrix for each model needs to be calculated for the controllability analysis before moving onto the controller gain design. In this research, the system models described in Eqs. (11)-(13) are composed of six state-space variables, which means the system is fully controllable when Rank($\boldsymbol{C}$) = 6, where the matrix of controllability test:

$$\boldsymbol{C} = [\boldsymbol{B}(\boldsymbol{x}) \vdots \boldsymbol{A}(\boldsymbol{x})\boldsymbol{B}(\boldsymbol{x}) \vdots \boldsymbol{A}(\boldsymbol{x})^{\boldsymbol{2}}\boldsymbol{B}(\boldsymbol{x}) \vdots \boldsymbol{A}(\boldsymbol{x})^{\boldsymbol{3}}\boldsymbol{B}(\boldsymbol{x}) \vdots \boldsymbol{A}(\boldsymbol{x})^{\boldsymbol{4}}\boldsymbol{B}(\boldsymbol{x}) \vdots \boldsymbol{A}(\boldsymbol{x})^{\boldsymbol{5}}\boldsymbol{B}(\boldsymbol{x})]. \tag{29}$$

Significantly, the state variables $\boldsymbol{x_3}$, $\boldsymbol{x_4}$ and $\boldsymbol{x_6}$ in Eqs. (11)-(13) are varied in matrices $\boldsymbol{A}(\boldsymbol{x})$ and $\boldsymbol{B}(\boldsymbol{x})$; therefore, the controllability test can be plotted from these state variables, as presented in Tables I and II.

TABLE I. THE CONTROLLABILITY TEST RESULTS FOR MODELS A, B AND C

Model	Controllability Test-3D	Controllability Test-2D (when x_6 is fixed at x_6= 0)	Controllability Test-2D (when x_3 is fixed at x_3= 0)	Controllability Test-2D (when x_4 is fixed at x_4= 0)
A	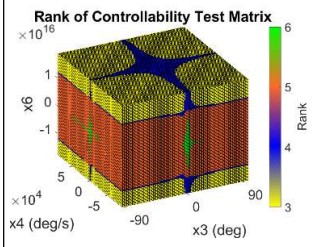	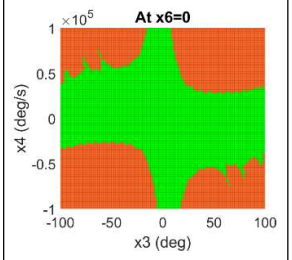	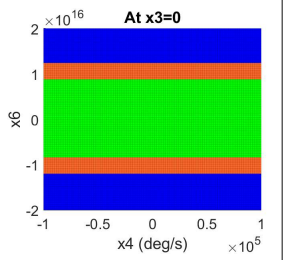	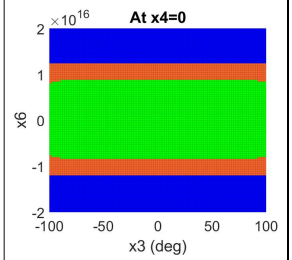
B	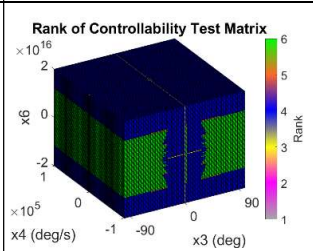	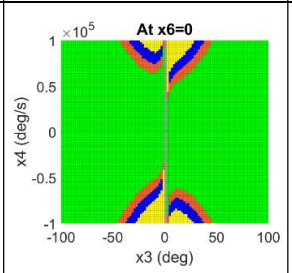	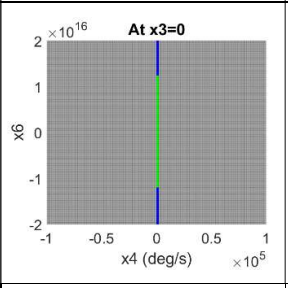	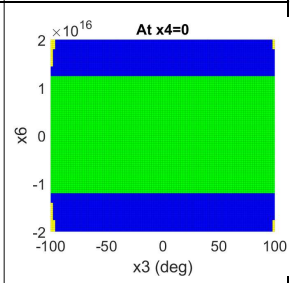
C	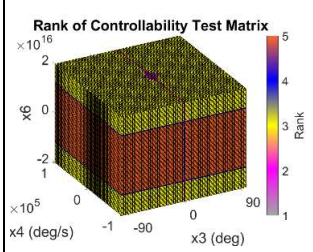	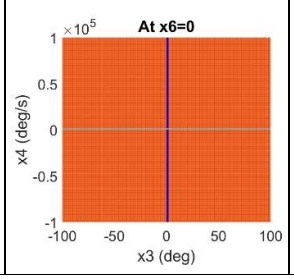	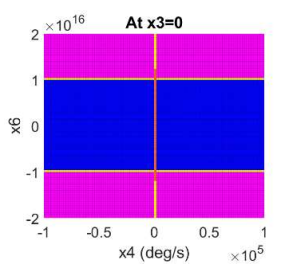	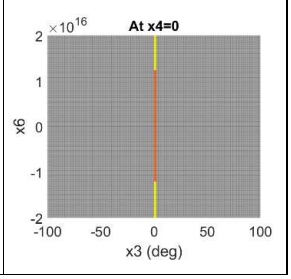

TABLE II. THE CONTROLLABILITY TEST RESULTS FOR A COMBINED SYSTEM MODEL AB

Model	Controllability Test-3D	Controllability Test-2D (when x_6 is fixed at x_6= 0)	Controllability Test-2D (when x_3 is fixed at x_3= 0)	Controllability Test-2D (when x_4 is fixed at x_4= 0)
AB	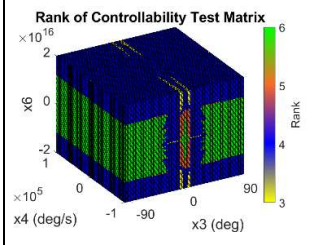	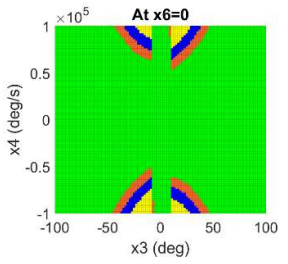	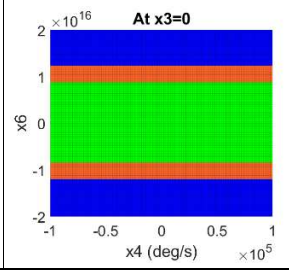	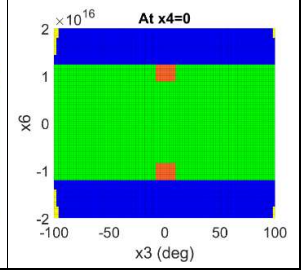

Table I. presents the ranks of controllability test matrices from Model A, B and C. The 2nd column shows the 3D plots in terms of 3 state variables, $\boldsymbol{x_3}$, $\boldsymbol{x_4}$ and $\boldsymbol{x_6}$. Moreover, the 2D plots in the 3rd – 5th columns illustrate cross-sections of the 3D graph of each axis by setting state variables $\boldsymbol{x_6}$, $\boldsymbol{x_3}$ and $\boldsymbol{x_4}$ to 0s, respectively. Note, the fully controllable region of the system, where Rank($\boldsymbol{\mathcal{C}}$)=6, is demonstrated in green.

It can be seen in the 3rd column of Model A that the completely controllable area is presented between -7° to 10°, approximately on the $\boldsymbol{x_3}$ axis; by contrast, Model B is not fully controllable when state variable $\boldsymbol{x_3}$ is close to 0°, and the green area lies on two sides of the $\boldsymbol{x_3}$=0° vertical line. Furthermore, in the 4th column of Model A and B, Model A shows a much larger fully controllable (green) region than Model B (which is only controllable around a small region near $\boldsymbol{x_4}$=0°). Finally, the last column of both models demonstrates large regions of full controllability; however, Model B presents a wider green area in the $\boldsymbol{x_6}$ axis than Model A, at approximately $\boldsymbol{\pm 1.2 \times 10^{16}}$ units.

For Model C, there is no region that all state variables are fully controllable, as shown in all columns. It can be said that this state-space model is only partially controllable. (i.e., Rank($\boldsymbol{\mathcal{C}}$) < 6) for all values of state variables $\boldsymbol{x_3}$, $\boldsymbol{x_4}$ and $\boldsymbol{x_6}$.

Next, a new model, named AB, is created by combining fully controllable regions of Model A and Model B. In this case, Model A is selected when the state variable $\boldsymbol{x_3}$ is between -10° and 10°; outside this range, Model B is selected for operation instead. The controllability tests for the new

Model AB are conducted in MATLAB and the rank calculation results are presented in Table II. Significantly, it can be seen from Column 3 that the central area near $\boldsymbol{x_3}$=0° is now completely controllable. Moreover, the wider fully controllable range in the $\boldsymbol{x_6}$ axis of Model B, instead of Model A's, is applied to the new system AB, as shown in the last column.

B: Maximum Initial Pitch Angle Simulation

In this subsection, system models A, B and AB will be used for stabilisation comparison in MATLAB simulation, when nonlinear optimal controllers are applied to them. Model C is not selected for controller application because there is no completely controllable area for state variables $\boldsymbol{x_3}$, $\boldsymbol{x_4}$ and $\boldsymbol{x_6}$ and therefore a state-space based nonlinear optimal controller cannot be designed to stabilise the unstable system described by Model C. Next, NFOC designs will be applied to Models A, B and AB to balance the TWR starting from different initial pitch angles $\boldsymbol{x_3}$ to reach and then maintain at the upright position. The maximum initial pitch angles achievable from these models are given in Figs. 2-4.

Fig. 2 presents the TWR balancing results from the initial pitch angle $\boldsymbol{x_3}$=14.1° of all three models. This angle is in fact the maximum initial pitch angle Models A and B can reach for stabilising control, but this is not the case for Model AB. Notably, there are high frequency oscillations in Model B's state variable evolutions when converging to reference positions because the system is not fully controllable when $\boldsymbol{x_3}$ is close to 0°, as discussed in the controllability test subsection earlier.

Additionally, when increasing the initial pitch angle $\boldsymbol{x_3}$ to 14.2°, the TWR Models A and B cannot be stablised, as shown in Fig. 3. Note, the $\boldsymbol{x_6}$ graphs of Model A and B reach beyond $\pm\mathbf{10^{19}}$, which exceed the fully controllable region (~$\pm\mathbf{10^{16}}$) as shown in columns 4-5 of Table I.

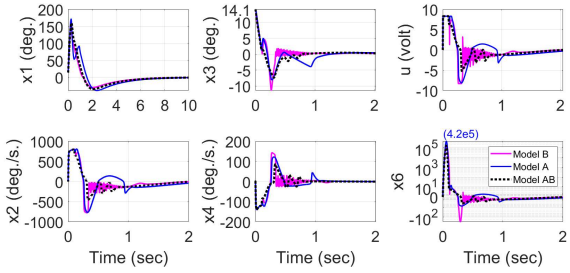

Fig.2. The stabilisation of Model A, B and AB at the initial pitch angles $\boldsymbol{x_3}$ = 14.1°

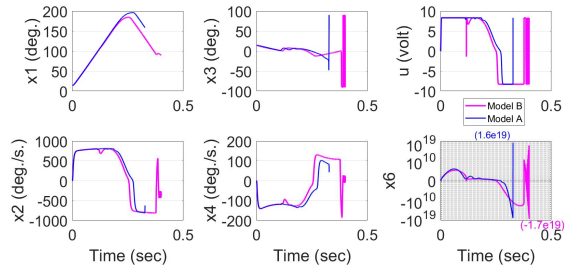

Fig.3. Unstable systems responses of Model A and B at the initial pitch angles $\boldsymbol{x_3}$ = 14.2°

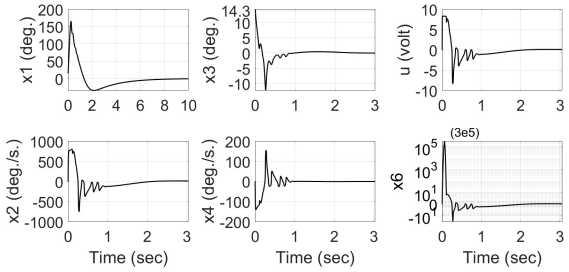

Fig.4. The stabilisation of Model AB at a larger initial pitch angle $\boldsymbol{x_3}$ = 14.3°

For Model AB, all state variable and control evolution graphs show smoother and faster to converge responses than Models A and B, in Fig. 2. Furthermore, this model presents capability of starting from a slightly wider pitch angle than Models A and B, at 14.3°, as demonstrated in Fig. 4. However, the oscillatory signals from Model B have affected Model AB to also show some oscillations in Fig. 4.

V. PRACTICAL IMPLEMENTATION RESULTS

Following on from controllability tests and nonlinear optimal controller simulations, the NFOC with EKF will be applied to a practical TWR, aided by SIMULINK programme in MATLAB. The block diagram of the controller structure is illustrated in Fig.5 and further specification details of the LEGO EV3 can be found in [5].

In this section, the LEGO TWR will apply NFOC feedback gains with EKF from different models, i.e., Models A, B and AB. A look-up table is used to store the feedback gain data to reduce calculation time from the LEGO EV3 programmable brick and to facilitate smoother control.

A partial look-up table of nonlinear optimal controller gains for Model AB is given in Table III. As one would expect, the feedback gains are higher when increasing the state variable x_3 for balancing the TWR; for instance, the control gain vector at x_3=0° against x_3= -20° in the 2nd column of Table III (when x_4= -120°/s) indicates the gain K_{13} (used to control the pitch angle) to be different by ~5.2.

Furthermore, the implementation result using Model AB shows a maximum initial pitch angle of x_3 = 20°, which is a wider operation range than the Model A (x_3 = 18°) to stabilise the TWR in the upright vertical as presented in Figs. 6 and 8. This is similar to the simulation result, where Model AB gains a higher initial pitch angle than Model A because combining Model A and Model B widens the overall controllable area and shows particular benefit when the pitch angle x_3 is increased, as presented in Section IV A.

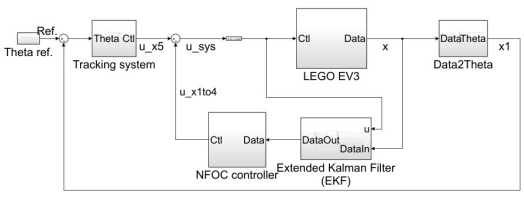

Fig.5. Simulink block diagram for stabilising the LEGO EV3 robot, using Nonlinear Freezing Optimal Control

TABLE III. THE PARTIAL LOOK-UP TABLE OF NONLINEAR MATRIX GAIN $\boldsymbol{K}$ (MODEL AB)

$x_3 \backslash x_4$	-120°/s	-20°/s	0°/s	20°/s	120°/s
-20°	[-1.382, -1.425, -54.593, -7.393, -0.5]	[-1.383, -1.427, -57.038, -7.415, -0.5]	[-1.383, -1.427, -57.579, -7.419, -0.5]	[-1.383, -1.428, -58.137, -7.422, -0.5]	[-1.383, -1.427, -61.173, -7.432, -0.5]
-10°	[-1.391, -1.450, -60.546, -7.249, -0.5]	[-1.391, -1.449, -60.368, -7.245, -0.5]	[-1.391, -1.449, -60.435, -7.260, -0.5]	[-1.391, -1.449, -60.297, -7.243, -0.5]	[-1.391, -1.448, -60.120, -7.239, -0.5]
0°	[-1.391, -1.449, -59.848, -7.168, -0.5]	[-1.391, -1.449, -59.848, -7.168, -0.5]	[-1.391, -1.449, -59.848, -7.168, -0.5]	[-1.391, -1.449, -59.848, -7.168, -0.5]	[-1.391, -1.449, -59.848, -7.168, -0.5]

By contrast, Model B cannot be stabilised by using a NFOC even though the initial pitch angle is set at the balancing position, i.e., $x_3 = 0°$ as shown in Fig.7. This matches the controllability test result for Model B, which shows the region near $x_3 = 0°$ is not fully controllable.

In the end, the maximum initial pitch angles achievable using NFOC from all models are summarised in Table IV.

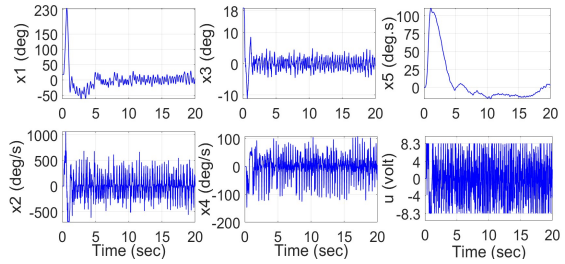

Fig.6. The stabilisation of Model A at the maximum initial $\boldsymbol{x_3} = 18°$

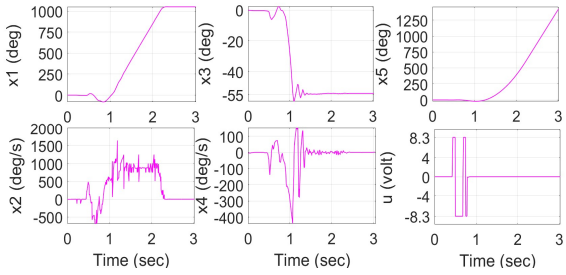

Fig.7. Unstable Model B at the initial pitch angles $\boldsymbol{x_3} = 0°$

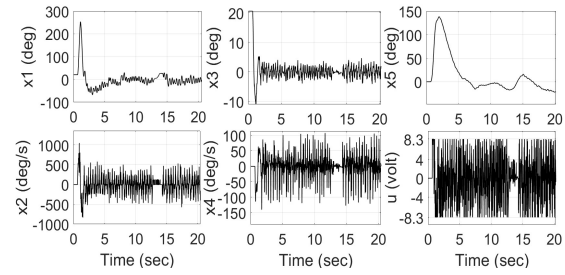

Fig.8. The stabilisation of Model AB at the maximum initial $\boldsymbol{x_3} = 20°$

TABLE IV. SUMMARy OF MAXIMUM INITIAL PITCH ANGLES

	Model A	Model B	Model C	Model AB
Simulation	14.1°	14.1°	Unstable	14.3°
LEGO EV3 Implementation	18°	Unstable	Unstable	20°

VI. CONCLUSIONS

In this paper, the controllability test is conducted to investigate the suitability of an advanced nonlinear optimal control technique for the control objective of balancing a TWR with different nonlinear state-space models. In particular, a novel mixing approach, combining two models based on their fully controllable regions, was introduced and analysed. Both simulation and implementation results demonstrated that the new model AB could be controlled by the NFOC with EKF from a larger initial pitch angle to reach and maintain at the vertical position, with faster and less oscillatory responses, comparing against Model A and model B. This approach opens up a new research direction of the impact study of mathematical models on controllability and control performance.

ACKNOWLEDGMENT

The first author would like to thank the Synchrotron Light Research Institute (SLRI) (public organisation), Thailand and the Royal Thai Government for the scholarship funding.

REFERENCES

[1] S. Banks, & K. Mhana, "Optimal control and stabilisation for nonlinear system," *IMA Journal of Mathematical Control and Information*, vol. 9, no. 2, pp 179-196, June 1992.

[2] R. F. Harrison, "Asymptotically optimal stabilising quadratic control of an inverted pendulum." *IEE Proceedings-Control Theory and Applications,* vol.150, no.1, pp.7-16, January 2003.

[3] X. Xu, H. Zhang, & G. Carbone. "Case studies on nonlinear control theory of the inverted pendulum," *In Inverted pendulum: from theory to new innovations in control and robotics*. O. Boubaker and R. Iriarte, eds. London, UK: IET, 2017, pp 225-262.

[4] S. Kokkrathoke, A. Rawsthorne, H. Zhang, and X. Xu, "Nonlinear Optimal Stabilising Control of a Two-wheel Robot," *International Journal of Modelling, Identification and Control.*, in press.

[5] S. Kokkrathoke, X. Xu, "Implementation of Nonlinear Optimal Control of Two-wheel Robot with Extended Kalman Filter," *IEEE International Conference on Automatic Control and Intelligent Systems (I2CACIS2021)*, Shah Alam, Malaysia, pp-19-25, June 26, 2021.

[6] T. Çimen and S. P. Banks, "Global optimal feedback control for general nonlinear systems with nonquadratic performance criteria," *Systems & control letters*, vol. 53, no. 5, pp. 327–346, May 2004.

[7] T. Çimen and A. . Merttopçuoğlu, "Asymptotically Optimal Nonlinear Filtering: Theory and Examples with Application to Target State Estimation," *IFAC Proceedings Volumes*, vol. 41, no. 2, pp. 8611–8617, July 2008.

[8] Y. Batmani and H. Khaloozadeh, "Optimal chemotherapy in cancer treatment: state dependent Riccati equation control and extended Kalman filter: Optimal Chemotherapy in Cancer Treatment," *Optimal control applications & methods,* vol. 34, no. 5, pp. 562–577, Sep. 2013.

[9] M. H. Korayem, N. Y. Lademakhi, and S. R. Nekoo, "Application of the state‐dependent Riccati equation for flexible‐joint arms: Controller and estimator design," *Optimal control applications & methods*, vol. 39, no. 2, pp. 792‐808, March 2018.

[10] Y. Yamamoto, "NXTway-GS (Self-Balancing Two-Wheeled Robot) Controller Design)." Mathwork.com. https://www.mathworks.com/matlabcentral/fileexchange/19147-nxtway-gs-self-balancing-two-wheeled-robot-controller-design (accessed Feb. 1, 2021).

[11] K. Ogata, *Modern control engineering*, 5th ed., London, UK: Pearson, 2009.

[12] L. Frank, L. Xie, & D. Popa, *Optimal and Robust Estimation With an Introduction to Stochastic Control*. Florida, USA: CRC Press, 2007